Cell Reports
Physical Science

Article

Catalytic resonance theory for the kinetic signatures of multiple wavelength photocatalysis

Graphical abstract

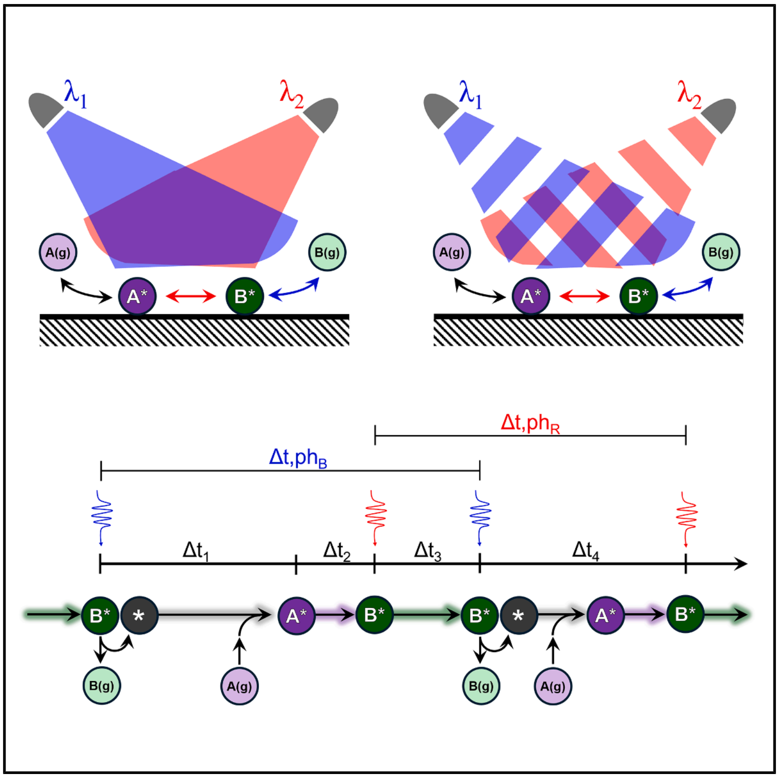

Highlights

- Two wavelengths of light maximally accelerate photocatalysis
- A non-dimensional photocatalytic map identifies the regions of high quantum yield

Authors

Jesse R. Canavan, Arik Beck,
Paul J. Dauenhauer

Correspondence

hauer@umn.edu

In brief

Photocatalysis that promotes more than one elementary reaction step using one or more wavelengths of light exhibits unique characteristics of photocatalytic rate acceleration. Canavan et al. show that surface chemistry achieves maximum kinetic rate enhancement when the two slowest steps in the catalytic mechanism are accelerated independently.

Canavan et al., 2026, Cell Reports Physical Science *7*, 103306
May 20, 2026 © 2026 The Author(s). Published by Elsevier Inc.
https://doi.org/10.1016/j.xcrp.2026.103306

Cell Reports
Physical Science

CellPress
OPEN ACCESS

Article

Catalytic resonance theory for the kinetic signatures of multiple wavelength photocatalysis

Jesse R. Canavan,[1,2] **Arik Beck,**[3] **and Paul J. Dauenhauer**[1,2,4,*]
[1]Center for Programmable Energy Catalysis (CPEC), University of Minnesota, 421 Washington Ave. SE, Minneapolis, MN 55455, USA
[2]University of Minnesota, Department of Chemical Engineering & Materials Science, 421 Washington Ave. SE, Minneapolis, MN 55455, USA
[3]Institute of Catalysis Research and Technology, Karlsruhe Institute of Technology, Hermann-von-Helmholtz-Platz 1, 76344 Eggenstein-Leopoldshafen, Germany
[4]Lead contact
*Correspondence: hauer@umn.edu
https://doi.org/10.1016/j.xcrp.2026.103306

SUMMARY

Multi-step surface chemistry promoted with one or two wavelengths of light exhibited distinct kinetic signatures indicative of the light-adsorbate interactions and the number of photon-sensitive elementary steps. In this work, kinetic Monte Carlo simulations identified the kinetic response of general surface mechanisms to variation in the per-site photon flux of one or two wavelengths of incident light. Photocatalytic rates were described via a non-dimensional photon flux, identifying multiple kinetic regimes with unique degrees of rate control. Under photon-controlled kinetic conditions, maximum quantum yield and turnover frequency were obtained under constant illumination, while pulsing of one or more light sources was shown to exhibit slower rates and less efficient photocatalytic promotion due to the inherent dynamic nature of light, which comprises a stream of photons. Simulations provided distinct kinetic signatures in catalytic rates and Arrhenius kinetics for specific light-surface-adsorbate interactions corresponding to photocatalytic promotion of specific steps in surface chemistry.

INTRODUCTION

The catalytic promotion of surface chemistry by the design of active sites exhibits a maximum at the Sabatier limit, which occurs for catalyst structures that match the rates of the two slowest elementary catalytic steps.[1–3] To overcome the static catalyst rate limitation, a proposed kinetic mechanism imposes a periodic stimulus that modulates the catalyst between rate-limiting steps identified as oscillating transitions in the catalytic degree of rate control.[4,5] Modifying the electronic properties of the catalyst active site requires external stimuli,[6,7] including the condensation of charge,[8,9] the imposition of electric fields,[10,11] the application of surface strain,[12,13] or the illumination of the active site.[14,15] Each catalytic stimulus exhibits unique scaling behaviors and kinetic implications for surface chemistry.

Illumination of the active site, i.e., photon-driven catalysis, is often described as a process akin to photolysis, where an incident photon enables the occurrence of an elementary reaction step on short timescales. These timescales, in the range of femtoseconds to picoseconds, are much faster than elementary reaction steps. Consequently, light, as an external stimulus, will result in different signatures than other stimuli, which perturb elementary steps on different timescales. Recent kinetic Monte Carlo (kMC) simulations of photon-promoted heterogeneous catalysis have examined the kinetics of light-accelerated desorption of surface reaction products using a single-wavelength light source.[16] As depicted in Figure 1A, a photon of blue light promotes desorption of product B* to B(g), while all other elementary steps of adsorption (A(g) to A*) and surface reactions (A* to B*) proceed thermocatalytically. The rate of catalyst stimulation via light was set by the photon arrival frequency, defined as the site-normalized photon flux, which can achieve arrival frequencies as high as 1,000 Hz for a light source with power of ∼2 W/cm^2.[14,17]

$$f_{arrival} = \frac{photon\ flux}{site\ areal\ density}\ [=]\ s^{-1} \qquad \text{(Equation 1)}$$

It is important to note that the arrival frequency $f_{arrival}$—e.g., for experimental continuous-wave (CW) illumination—is an average frequency, and the intervals between two incident photons are of a stochastic nature. Absorption of a photon and associated kinetic promotion are extremely short events[17–19]; for photon arrival frequencies as high as ∼1,000 Hz (∼2 W/cm^2),[14,17] surface thermochemistry occurs for the majority of the duration of time. Consequently, the studied catalytic situation cannot be described solely in terms of conventional photochemistry, where catalytic turnover is usually exclusively dominated by quantum yields (QYs); the reaction can be controlled by either thermocatalytic or photocatalytic elementary steps, depending on the illumination and thermal conditions. Characterization of the

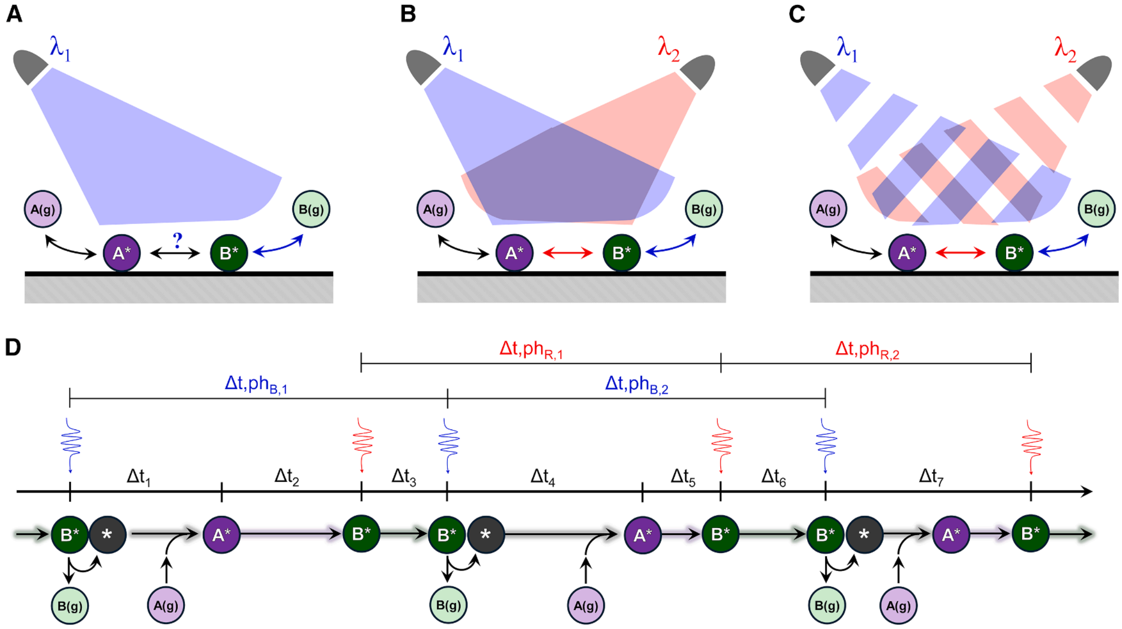

Figure 1. Multi-step promotion via photocatalysis

(A) The generic reaction of A(g) to B(g) via surface species A* and B* is accelerated by a single wavelength of light, λ_1, promoting desorption of B*.

(B) Two selected wavelengths of light, λ_1 and λ_2, are selected to accelerate independent elementary reaction steps of surface reaction, red, and desorption of B*, blue.

(C) The two selected wavelengths of light are pulsed in time.

(D) The sequence of blue and red photons interacting with stochastic surface chemistry occurs with defined temporal increments.

Data are available in Table S1.

utilization of light in this work considers the internal QY (IQY), defined as the moles of a product produced relative to the moles of absorbed photons,[20] as well as the IQYs of elementary steps $IQY_{A,ads}$, $IQY_{A\rightarrow B}$, and $IQY_{B,des}$. Not all absorbed photons will promote chemistry; some photons will be absorbed and generate heat, thereby reducing the IQY. Nevertheless, simulations indicated that surface reactions with photon sensitivity to desorption can be accelerated orders of magnitude beyond the Sabatier limit, albeit for photocatalytic materials with electronic characteristics far from the Sabatier maximum.[16] As the Sabatier volcano's shape derives from two catalytic rate limitations, accelerating only one elementary step (e.g., desorption) with a single wavelength light provides only a limited method of accelerating the overall reaction.

A single wavelength light source could promote the kinetics of a single elementary step (e.g., desorption), but it is also possible for the same light source to accelerate multiple reaction steps, such as desorption and intermediate decomposition (e.g., A* to B*). Surface species that can desorb to a stable gas-phase species are detectable by gas-phase sampling; desorption of CO* to CO(g) can be both measured and modeled under illumination with 440 nm light.[17] Alternatively, measuring the light-surface-adsorbate interaction of surface reactions (e.g., A* to B*) requires surface coverage characterization by methods such as infrared spectroscopy. As an example, methyl formate decomposition was shown to include the elementary reaction of formate (HCOO*) decomposition to CO* and OH* on Pt/TiO$_2$ promoted with visible light.[21]

While elementary steps promoted by light that occur entirely on a surface (e.g., A* to B*) are not immediately detectable, their kinetic influence on gas or liquid products is measurable and distinct from other photon-promoted reactions. In this work, the kinetics of photon-promoted catalysis was evaluated to assess the kinetic influence of light on multiple elementary steps. In particular, the initial question concerns the kinetic implications of a single wavelength of light (Figure 1A) that can accelerate the rate of the two rate-controlling steps. An alternative mechanism utilized two different wavelengths of light (λ_1 and λ_2) that were applied at independent varying fluxes (Figure 1B). Finally, additional programmable control of independent light sources included the pulsing of light beams incident to the catalyst surface coordinated with the parameters of the duty cycle, $0 < DC < 1$, defined as the fraction of each illumination cycle of λ_1 (blue) light, and coordination frequency, f_{coord}, defined as the frequency of switching between the different light wavelengths (Figure 1C).

RESULTS

kMC model and simulation development

The scenarios presented in Figure 1 were evaluated with the kMC method using both variable-time-step and fixed-time-step methods. As depicted in Figure 1D, the variable-time-step kMC method implemented the kinetic model shown in Figure 2A (also Figure S1), with an A(g)-to-B(g) reaction occurring reversibly on a surface through intermediates A* and B*.

Simulation code is provided in Figures S2 and S3. Kinetic parameters associated with thermochemical steps were determined from linear scaling behaviors between surface intermediates ($\gamma = 3$, $\delta = 0.7$ eV) and transition state energy linear scaling ($\alpha = 0.7$, $\beta = 0.9$ eV).[22–24] Scaling parameters were selected as moderate values representing common chemical systems.[5,25] To these thermochemical steps were added unidirectional photocatalytic steps with their respective IQYs ($IQY_{A,ads}$, $IQY_{A\rightarrow B}$, and $IQY_{B,ads}$) of 100% for this specific elementary step to desorb B* to B(g) via λ_1 and convert A* to B* via λ_2; it was assumed that the kinetics for these steps were temperature independent. Recent experimental evidence on the desorption of CO* from Pt catalysts has demonstrated that the photo-desorption kinetics are substantially less affected by temperature than thermocatalytic reactions; however, the apparent QY at 440 nm for CO* photo-desorption showed a weak temperature dependence (~0.2 eV).[17] This dependence was not considered here, and we are aware that the present simulations present idealized cases. In each state of the catalytic cycle (A*, B*, or *), the time step (Δt_n) and the selected pathway were determined by stochastically weighting the kinetics of each elementary step, as described by Gillespie and co-workers.[26–28] Complete kinetic model and simulation details are available in the supporting information.

The selected model was deliberately highly idealized to identify and communicate only the controlling kinetic elements of photo- and thermochemistry. While the mechanism only accounts for three steps of adsorption (A(g) to A*), surface reaction (A* to B*), and desorption (B* to B(g)), real chemistries can be multi-step with a network of series and parallel reactions. Diffusion through an external boundary layer above the catalyst surface was not included in the model, although it can potentially become rate limiting in real catalytic applications.[29,30] Both thermal- and photo-excited steps were based on Arrhenius rate expressions that account for the probability of specific events, as used in prior work.[16] In addition, all steps are unimolecular, with each surface species only occupying a single catalyst site. For this reason, spatial information was not included in the model, such as multiple types of sites (e.g., terrace, step, and corner sites) or lateral interactions associated with neighboring occupied catalyst sites.[31,32] For this reason, the simulated model is highly idealized for the purpose of only providing insight into general overall catalytic behaviors; future models describing real reactions will include these additional model complexities.

Reaction acceleration by a single wavelength of light ($\lambda_1 = \lambda_2$)

The selected reaction exhibits a Sabatier volcano under thermocatalytic conditions (zero illumination), depicted in Figure 2B (and Figure S4) with a maximum turnover frequency $(TOF)_B$ of 2.75 s^{-1} at a binding energy, BE_B, of 0.82 eV at 343 K. In this reaction, TOF_B is limited by the rate of B* desorption for $BE_B > 0.82$ eV and limited by the surface reaction (A* → B*) for $BE_B < 0.82$ eV. The photocatalytic reaction was simulated using the variable-time-step method under CW illumination with only a single wavelength, which stimulated both rate limitations ($\lambda_1 = \lambda_2$). As shown in Figure 2B, the photon arrival frequency was varied over four orders of magnitude ($0.1 < f_{arrival} < 1,000$ Hz). For $f_{arrival}$ of 3 Hz or greater, the resulting TOF_B exceeded the Sabatier maximum of 2.75 s^{-1} for all possible simulated materials ($0.6 < BE_B < 1.0$ eV). At lower photon arrival frequencies ($f_{arrival} < 3$ Hz), the TOF_B decreased on either side of the Sabatier maximum.

Catalytic rate acceleration with CW illumination of a single wavelength that promoted both reaction steps (A* → B* and B* → B(g)) was interpretable via the parity plot between TOF_B and the photon arrival frequency shown in Figure 2C. Parity in this case implied that a single photon equals one catalytic turnover—thus an IQY of 100%. At low photon arrival frequencies, the TOF_B exhibited the thermocatalytic rate with negligible photon-promoted rate enhancement, resulting in an IQY of approximately zero. However, TOF_B became proportional to the photon arrival frequency near the parity line, increasing the turnover for incident photons (i.e., first-order rate dependence on photons); see Figure S6A for light rate order calculations. This parity behavior perfectly describes the experimentally observed linear dependence of photon flux on rate enhancement through illumination.[33] While nearly equal to parity at high photon arrival frequencies, a ~50% difference in TOF_B from parity indicated a ratio of two photons per catalytic turnover and an IQY of ~50%. The "external QY" (EQY) that relates the fraction of catalytic turnovers relative to the number of photons delivered from an external light source was not used in this work.[34–36]

The utility of photons in driving reactions was apparent when calculating the ratio of TOF_B to photon arrival frequency; this determined the rate of catalytic turnover relative to the rate of photons interacting with the catalyst surface. As visible in the TOF_B of Figure 2B at 1,000 Hz, the TOF_B was ~1,000 s^{-1} for a BE_B of 0.6 eV and then decreased to ~500 s^{-1} for $BE_B > 0.7$ eV. This was consistent with a shift in the reaction requiring only one photon per catalytic turnover at a BE_B of 0.6 eV to requiring two photons per catalytic turnover at $BE_B > 0.7$ eV; the IQY changed accordingly from ~90% to ~50%, as shown in Figure S6. At a low BE_B of 0.6 eV, the thermocatalytic reaction was primarily limited by the surface reaction (A* → B*), while the rate of B* desorption was fast; only one photon was necessary to accelerate this reaction for the selected photon arrival frequencies. Alternatively, for BE_B near the Sabatier maximum, both elementary steps (A* → B* and B* → B(g)) were rate controlling, and two photons were necessary to accelerate the reaction beyond the Sabatier limit. Finally, for high-BE_B materials, the reaction was limited only by the rate of desorption, and again, only one photon was necessary. This is visible in Figure 2B for the 10 and 30 Hz photon arrival frequencies (shown in non-logarithmic scale in Figure S6C); TOF_B was a minimum for the BE_B of 0.85 eV and then increased for higher and lower values of BE_B.

The simulation results presented in Figure 2 indicated different illumination requirements to accelerate photocatalytic reactions for the three kinetic regimes identified by the Sabatier volcano. At extreme BE_B away from Sabatier maximum, the thermocatalytic reaction was limited by only one elementary step; only a single photon was necessary to accelerate that rate-controlling step (surface reaction at low BE_B and product desorption at high BE_B). The intermediate kinetic regime occurred within the inverted volcano at moderate BE_B values; the inverted volcano is

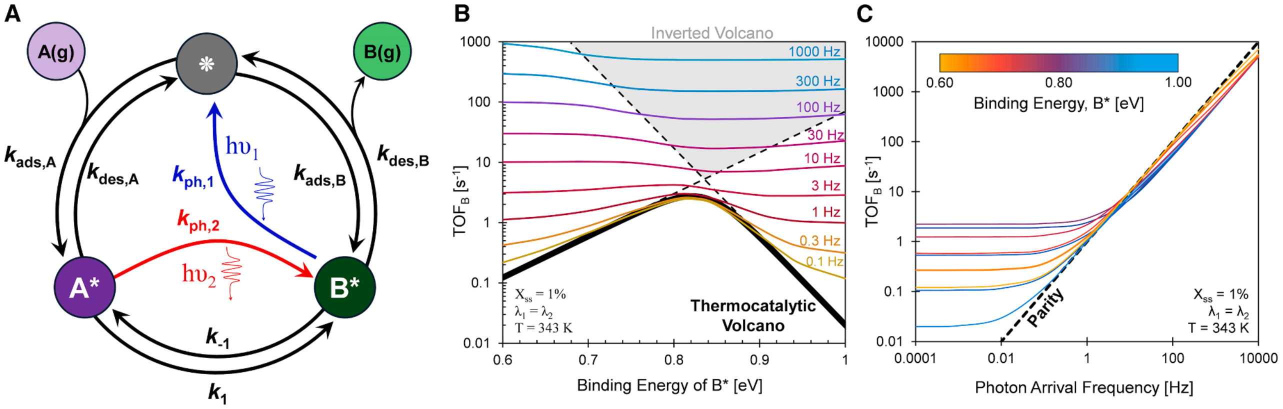

Figure 2. Kinetics of multi-step photocatalysis via a single-wavelength ($\lambda_1 = \lambda_2$) source

(A) A catalytic cycle converting A(g) to B(g) through surface intermediates A* and B* occurs through thermocatalytic steps (black) of adsorption, surface reaction, and desorption along with photon-promoted steps of surface reaction (blue) and desorption (red). Modeled kinetic parameters of thermochemical steps were calculated from linear scaling between surface intermediates (γ = 3, δ = 0.7 eV) and transition state energy linear scaling (α = 0.7, β = 0.9 eV).

(B) The static thermocatalytic reaction at 343 K, 100 bar, and 1% exhibits a Sabatier volcano with a maximum at BE_B of 0.82 eV and a TOF of 2.75 s^{-1}. Application of a stream of photons with a single wavelength ($\lambda_1 = \lambda_2$) that accelerates both photon-promoted steps ($k_{ph,1}$ and $k_{ph,2}$) for varying photon arrival frequencies ($0.1 \leq f_{arrival} \leq 1,000$ Hz) increases the catalytic turnover frequency (TOF_B).

(C) The TOF_B of catalyst surfaces described with different BE_B transitions, from independent of the photon arrival frequency to first-order dependence with increasing photon arrival frequency.

Data are available in Tables S2 and S3.

depicted in the gray region between the dashed lines of Figure 2B. Within this inverted volcano region, two photons were required to accelerate the catalytic reaction for photon arrival frequencies that exceeded the Sabatier maximum TOF_B.

The other key observation presented in Figure 2C is the absence, for this range of considered photon arrival frequencies, of a detectable resonance frequency, defined as the maximum of the effective catalytic rate.[5] TOF_B increased as the photon arrival frequency increased without a detected maximum over the range of ($0.1 < f_{arrival} < 10,000$ Hz). The two slowest thermochemical frequencies were associated with the surface reaction ($\tau_1 = k_1^{-1}$ and $f_1 = \tau_1^{-1}$) and B* desorption ($\tau_{desB} = k_{desB}^{-1}$ and $f_{desB} = \tau_{desB}^{-1}$), but both steps were accelerated with light as fast as photons arrived. In this case, the next slowest frequency was associated with adsorption of A(g) to form A*, which was a function of the reactant pressure and adsorption rate constant ($\tau_{adsA} = (k_{adsA}P_A)^{-1}$ and $f_{adsA} = \tau_{adsA}^{-1}$). The resonance frequency existed as the per-site flux of A(g) for f_{adsA} at $\sim 10^8$ Hz, identified as the maximum in the effective catalytic rate, as shown in Figure S6D. This flux-limited condition was about five orders of magnitude away from an achievable experimental system, which can only achieve photon arrival frequencies of $\sim 10^3$ Hz.

Photocatalysis at a single wavelength ($\lambda_1 = \lambda_2$) that promoted both surface reaction and surface product desorption was interpreted using an Arrhenius plot with unique kinetic features. As shown in Figure 3A (and Figure S5), the Arrhenius plot of photocatalysis with a material described with a BE_B of 0.80 eV for photon arrival frequencies of 10, 100, and 1,000 Hz exhibited only two kinetic regimes. At low temperatures, the TOF_B was a fixed value equal to exactly half of the applied photon arrival frequency ($TOF_B = 0.5\, f_{arrival}$), as each catalytic turnover was a two-photon process at these conditions. This kinetic regime resulted in a surface coverage that was equally split between coverage of A* and B* ($\theta_A = \theta_B = 0.50$) as shown in Figure 3B. The mechanism leading to a fixed value of TOF_B with temperature was interpreted via the degree of rate control (DRC) calculated from the kinetic sensitivity of each elementary step, S_i,[37,38]

$$S_i = \left(\frac{\partial ln(TOF_B)}{\partial ln(k_i)}\right)_{k_{i \neq j}}. \qquad \text{(Equation 2)}$$

The degree of rate control for each elementary step was then calculated as the sum of the forward and reverse sensitivities, $DRC_i = S_i + S_{-i}$,of each elementary step.[25,39] Alternatively, the degree of rate control of the photon arrival frequency determined the extent of kinetic control of the photon flux,[16,40]

$$DRC_f = \left(\frac{\partial ln(TOF_B)}{\partial ln\, f_{arrival}}\right). \qquad \text{(Equation 3)}$$

Depicted in Figure 3C, the degree of rate control of the low-temperature kinetic regime indicated complete kinetic control ($DRC_f \sim 1.0$) of the photon arrival frequency, $f_{arrival}$.; the reaction proceeded as fast as the photons arrived at the active site. In contrast, the high-temperature kinetic regime shown in Figure 3A occurred when the thermocatalytic TOF overtook the photon arrival frequency. At temperatures for this condition ($T^{-1} < \sim 0.0028$ K^{-1}), the reaction proceeded as if it were a thermocatalytic reaction for a material with BE_B of 0.8 eV; the surface coverage was higher in θ_A and lower in θ_B (Figure 3B). Moreover, the degree of rate control (Figure 3C) at higher temperatures was dominated by the surface reaction ($DRC_{A^* \leftrightarrow B^*} \sim 0.80$), while surface product contributed only minorly ($DRC_{B^* \leftrightarrow B(g)} \sim 0.20$); this was consistent with the selected material (BE_B = 0.80 eV) being slightly to the left of the Sabatier volcano peak (Figure 2B) under binding conditions that lead to more kinetic control associated with the surface reaction.

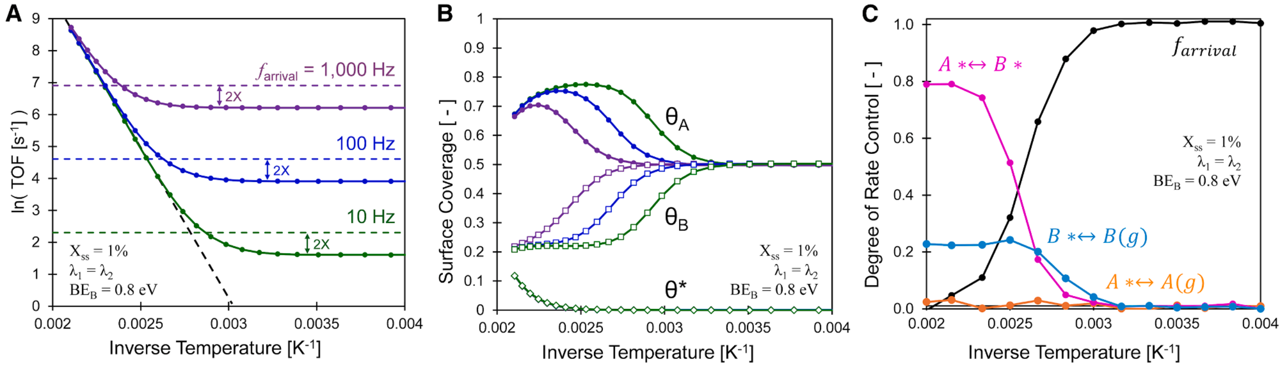

Figure 3. Characteristics of the idealized photocatalytic kinetics of a single-wavelength ($\lambda_1 = \lambda_2$) source

(A) The Arrhenius plot of the photocatalytic reaction A(g) to B(g) via intermediates A* and B* at varying temperatures, 100 bar total pressure, three photon arrival frequencies (10, 100, and 1,000 Hz), and 1% conversion for a material with BE_B of 0.8 eV. The single wavelength of light promotes the conversion of A* to B* as well as the desorption of B* to B(g).

(B) The associated surface coverages of A*, B*, and open sites, *.

(C) The degree of rate control associated with the photon arrival frequency, the transition state between A* and B*, and the two adsorption/desorption steps.

Reaction acceleration by two different wavelengths of light ($\lambda_1 \neq \lambda_2$)

The complexity of photocatalysis increased significantly when two different wavelengths of light ($\lambda_1 \neq \lambda_2$) independently accelerated different elementary reaction steps. As shown in Figure 1B, blue light (λ_1) promoted desorption of B* to B(g), while red light (λ_2) accelerated the surface reaction (A* to B*). Photocatalysis with two wavelengths of CW light incorporated three stochastic phenomena (surface thermochemistry and photon surface incidence of two wavelengths) with independent timescales (photon arrival frequency of λ_1, photon arrival frequency of λ_2, and the thermocatalytic TOF) that interacted to accelerate the overall rate of reaction. As depicted in Figure 1D for the variable-time-step kMC simulations, elementary steps proceeded with time steps Δt_n, which were predictable only on average; each individual step of adsorption, reaction, and desorption occurred on a timescale commensurate with the free energy of the transition and a degree of randomness (selected by a random number in the kMC method). On top of this thermochemical reaction, the arrival of blue (λ_1) or red (λ_2) photons occurred, promoting individual elementary steps.

An initial set of simulations of mixed-wavelength photocatalysis ($\lambda_1 \neq \lambda_2$) in Figure 4A (and Figure S8) indicated increased complexity between the applied intensity of λ_1 and λ_2 light sources and the resulting TOF_B. While fixing the λ_1 photon arrival frequency at $f_{arrival,1}$ = 350 Hz and varying the λ_2 photon arrival frequency ($10^{-3} < f_{arrival,2} < 10^4$ Hz), the TOF_B eventually achieved 350 s^{-1}. Alternatively, fixing the λ_1 photon arrival frequency at either 4.2 or 0.05 Hz never resulted in a TOF_B close to 4.2 or 0.05 s^{-1}; instead, the TOF_B at these two photon arrival frequencies both approached a similar value of ~17 s^{-1} (at high $f_{arrival,2}$), which was explainable in the following description of kinetic regions. The complete datasets of Figures 4A–4F are included in Tables S21–S33.

This photocatalytic complexity was interpreted using the more complete heatmap in Figure 4B, which depicted the TOF ($2.5 < TOF_B < 10^4$ s^{-1}) for varying $f_{arrival,1}$ and $f_{arrival,2}$. At a temperature of 343 K, the thermocatalytic TOF_B was ~2.5 s^{-1}, which is in the middle of the range of considered photon arrival frequencies. Figure 3A also indicated that this temperature (0.0029 K^{-1}) was in the transition region between light-controlled TOF_B and thermocatalysis-controlled TOF_B. The transition between controlling kinetics was defined by the dimensionless photon arrival frequency, $Ƒ_i = f_{arrival,i}/k_i$, which is the ratio of the photon arrival frequency of λ_i to the corresponding elementary step rate constant, k_i. As a BE_B of 0.8 eV was near the Sabatier volcano maximum, the k_1 of 2.9 s^{-1} was not too different from the k_{desB} of 17.6 s^{-1} on a log scale. On either side of this kinetic transition ($Ƒ_i$ = 1.0) were each of the kinetic regions: in region I of Figure 4B ($Ƒ_1 < 1$ and $Ƒ_2 < 1$), the TOF_B was controlled by the thermocatalytic rate (~2.5 s^{-1}), and in region IV ($Ƒ_1 > 1$ and $Ƒ_2 > 1$), the TOF_B was controlled by the photocatalytic stimulation ($f_{arrival,1}$ and $f_{arrival,2}$).

Regions II and III in Figure 4B were the mixed kinetic regimes. For example, in region III, the $f_{arrival,2}$ was greater than the rate of the surface reaction (k_1 = 2.5 s^{-1}), while $f_{arrival,1}$ was less than the B* desorption rate (k_{desB} = 17.6 s^{-1}), resulting in mixed dimensionless photon arrival frequencies ($Ƒ_1 < 1$ and $Ƒ_2 > 1$). In other words, in region III desorption was thermocatalytically controlled such that the maximum TOF_B was equal to ~17 s^{-1}, as previously shown in Figure 4A. Alternatively, in region II, the $f_{arrival,1}$ was greater than the rate of desorption (k_{desB} = 17.6 s^{-1}), while $f_{arrival,2}$ was less than the surface reaction rate (k_{desB} = 17.6 s^{-1}), with mixed dimensionless photon arrival frequencies ($Ƒ_1 > 1$ and $Ƒ_2 < 1$). As such, the overall TOF_B of region II was limited to ~2.5 s^{-1} by the surface reaction. The selection of the temperature determined the values of the reaction rate constants and the corresponding values of the dimensionless photon arrival frequencies ($Ƒ_1$ and $Ƒ_2$), thereby varying the extent of each kinetic region. When a low temperature of 250 K (0.004 K^{-1}) was simulated, the entire heatmap ($10^{-3} < f_{arrival,1}$ and $f_{arrival,2} < 10^4$ Hz) comprised region IV, as shown in Figure S7 (Tables S5–S20).

The catalyst surface coverages of A* (Figure 4C) and B* (Figure 4D) provided further insight into the controlling elementary steps and the role of light. In the thermocatalysis-controlled region I, the surface coverages were constant at θ_A ~ 0.8 and θ_B

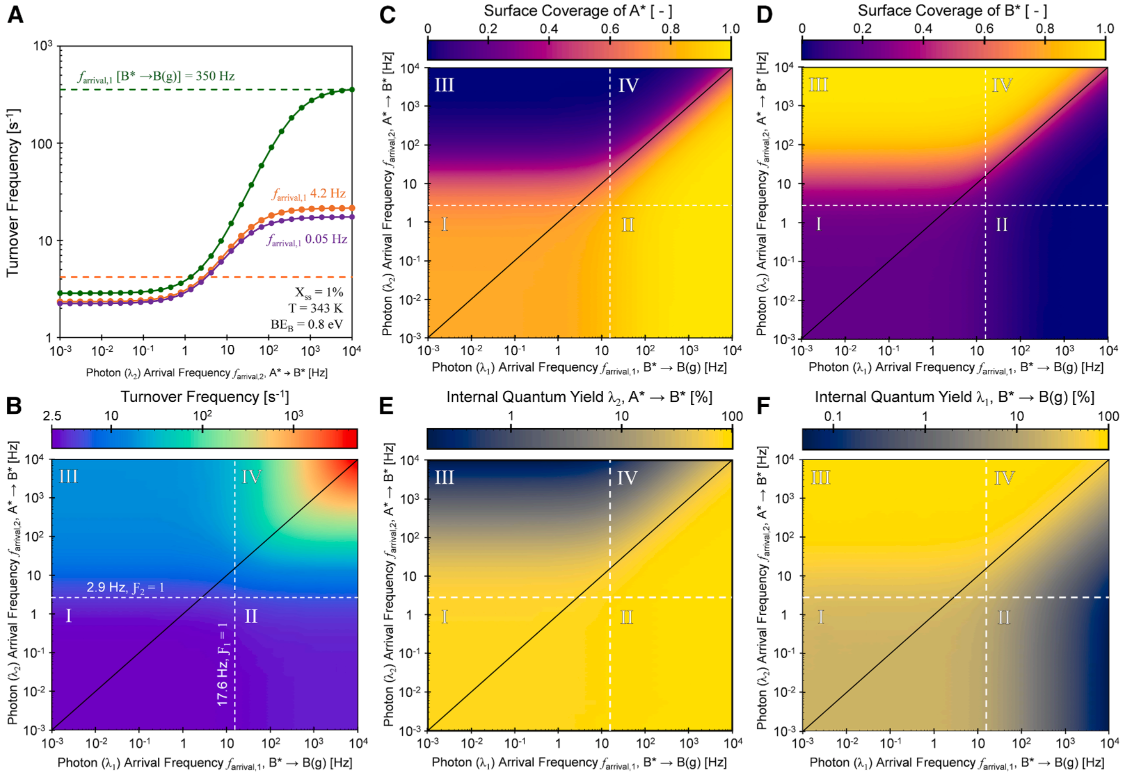

Figure 4. Idealized two-wavelength photocatalysis of the A(g)-to-B(g) reaction at 343 K

The photocatalytic reaction occurs via surface intermediates A* and B*, with photocatalytic acceleration of the surface reaction (A* → B*) and surface product desorption (B* → B(g)) occurring with two different sources of light, each providing a Poisson distribution of photons. All reactions occurred with a material having a BE_B of 0.8 eV, 343 K, 100 bar total pressure, and a conversion of 1%.

(A) The TOF for varying photon arrival frequency (A* → B*) for three arrival frequencies that accelerate surface product desorption (B* → B(g)).

(B–F) Heatmaps were generated for varying arrival frequencies of the two wavelengths for (B) TOF, (C) surface coverage of A*, (D) surface coverage of B*, (E) apparent quantum efficiency of the light that promotes A* → B*, and (F) apparent quantum efficiency of the light that promotes B* → B(g). The solid black line represents parity, while the white dashed lines identify the kinetic transitions defined by dimensionless photon arrival frequency, $F_i = f_{arrival,i}/k_i$. Heatmaps are divided into four quadrants, wherein (I) the thermocatalytic rate constants are higher than the photon arrival frequencies ($F_1 < 1$ and $F_2 < 1$), (IV) the photon arrival frequencies are higher than the thermocatalytic rate constants ($F_1 > 1$ and $F_2 > 1$), and (II and III) a mix of ratios of the thermocatalytic rate constants and the photon arrival frequencies.

Data are available in Tables S21–S33.

~ 0.2. This ratio of surface coverages was unequal because the selected BE_B of 0.8 eV was slightly to the left of the Sabatier maximum; desorption for this catalyst material was slightly faster than the surface reaction, resulting in higher coverages of A* than B*. This ratio of surface coverages shifted in the mixed regions II and III as one of the two wavelengths of light overtook the thermocatalytic rate, pushing these regions to either mostly covered in A* (region II) or mostly covered in B* (region III). Finally, in region IV, the light entirely determined the kinetics of the reaction, such that the parity line identified the transition between dominant photon arrival frequency ($f_{arrival,1}$ or $f_{arrival,2}$) and the associated surfaces primarily covered in A* or B*.

Interpreting the QY of the four regions of I–IV in Figure 4 required quantification of photon utility. Not all photons delivered to the catalyst surface promoted chemistry; some instead interacted with a site for which no chemical promotion occurred and generated heat. Simulations provided a quantitative method for assessing light-surface interactions and identifying kinetic behaviors and their transitions with varying illumination parameters, including intensity, wavelength, and coordination (e.g., pulsing or chopping of light sources). With independent thermochemistry, photons could interact with open sites, A*, or B*, such that they could deliver energy (i.e., heat) or promote a specific elementary step, such as desorption (B* to B(g)) or the surface reaction (A* to B*). Effective use of photons—high IQY—utilized one photon per turnover for systems for which a single elementary step, such as desorption, $Ph_{\lambda_1}[B* \rightarrow B(g)]$, or reaction, $Ph_{\lambda_2}[A* \rightarrow B*]$, was affected by light.

$$IQY_1 = \frac{Ph_{\lambda_1}[B* \rightarrow B(g)]}{all\ \lambda_1\ photons} = \frac{Ph_{\lambda_1}[B* \rightarrow B(g)]}{Ph_{\lambda_1}[B* \rightarrow B(g)] + Ph_{\lambda_1}[heat]} \quad \text{(Equation 4)}$$

$$IQY_2 = \frac{Ph_{\lambda_2}[A* \rightarrow B*]}{all\ \lambda_2\ photons} \quad \text{(Equation 5)}$$

The IQYs of wavelengths λ_1 and λ_2 were depicted in Figures 4E and 4F for each of the four kinetic regions. As shown, the IQY_i

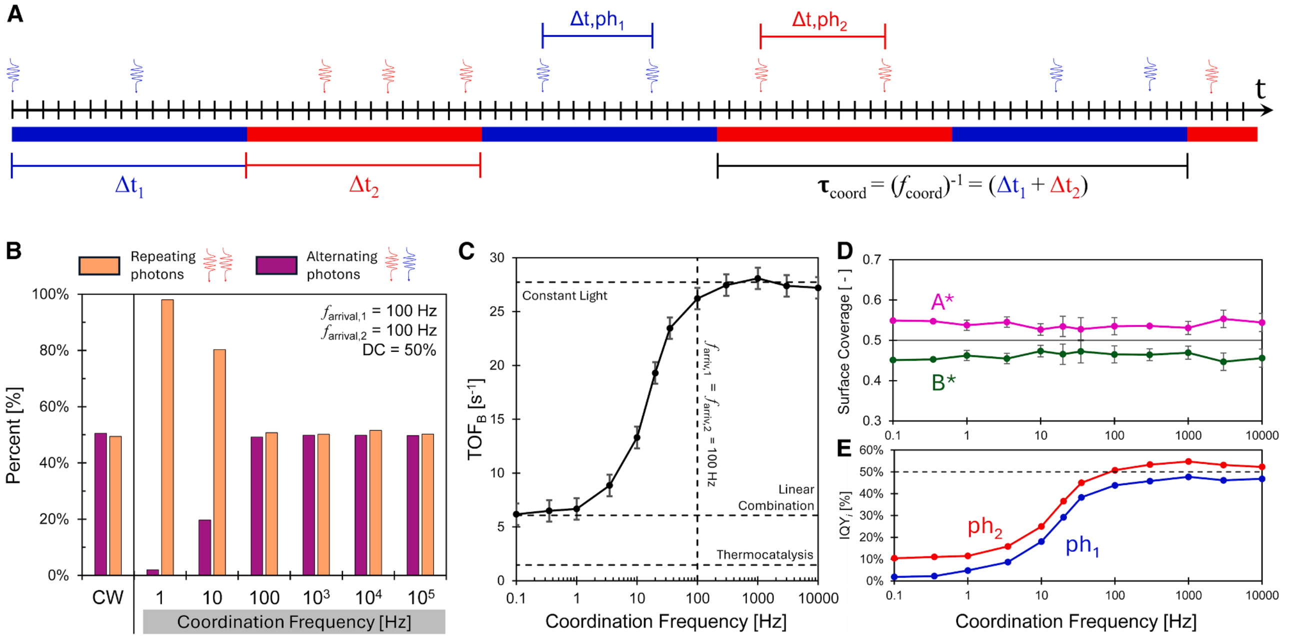

Figure 5. Coordinated multi-wavelength photocatalysis

(A) Light sources alternating between two wavelengths with coordination frequency, f_{coord}, over a period of two parts ($\tau_{coord} = \Delta t_1 + \Delta t_2$) with spacing between photons arriving at the surface of Δt,ph$_i$.

(B) The percentage of sequential photons that repeat (red then red or blue then blue) or alternate (red then blue or blue then red) for continuous-wave (CW) light sources and varying coordination frequency with a 50% duty cycle of red and blue photons both at 100 Hz arrival frequency.

(C–E) The TOF to form B(g), surface coverages, and photon efficiencies for varying two-wavelength coordination frequency at 338 K, 100 bar total pressure, 1% conversion, and photon arrival frequencies of 100 Hz for both light sources. All error bars represent a 99% confidence interval.

Data are available in Tables S34 and S35.

varied across the different regions for both wavelengths of light inversely to the photon arrival frequency of that particular wavelength. In region II, the $f_{arrival,1}$ was higher than the thermocatalytic rate, but the IQY_1 was low; conversely, the $f_{arrival,2}$ was higher in region III, but the IQY_2 was low. This inverse behavior exists across the entire heatmap shown in Figures 4E and 4F, such that the two IQYs always summed to the same number ($IQY_1 + IQY_2 = 100\%$). For both wavelengths, the total IQY was calculated by dividing the number of times the surface reaction and desorption steps were promoted by photons by the total number of delivered photons.

$$IQY_{total} = \frac{Ph_{\lambda_1}[B* \rightarrow B(g)] + Ph_{\lambda_2}[A* \rightarrow B*]}{All\ \lambda_1 + \lambda_2\ photons} \qquad \text{(Equation 6)}$$

Across the entire dataset for all conditions and kinetic regions, the IQY_{total} was 50%.

The origin of the 50% IQY_{total} from two-wavelength photocatalysis is derived from the stochastic nature of a continuous source of photons. As depicted in Figure 5A (and Figure S9), photons arrived at the surface as distinct events that could vary in sequence, with either alternating photons (e.g., red then blue or blue then red) or sequential photons (e.g., red then red or blue then blue). The sequence of photon wavelengths mattered for the chemistry, as ph$_2$(red) only accelerated the surface reaction and ph$_1$(blue) only promoted desorption. Two red photons in a row resulted in catalytic promotion of A* to B*, with the second red photon only generating heat. It was therefore desirable to control the sequence of imposed photons.

The fraction of photons that arrive at the surface alternating in wavelength (red then blue or blue then red) was determined as shown in Figure 5B. The basis for comparison was the CW illumination of the catalyst surface, which exhibited a 50% probability that each arriving photon would have a different wavelength from the preceding photon. A CW laser delivers photons to the surface, for which a sufficient sample size of photon temporal spacing exhibits a Poisson distribution.[41,42] Thus, the probability was equal that the next photon would be of the same or a different wavelength (when $f_{arrival,1} = f_{arrival,2}$).

Coordination of pulses of two different wavelengths of light ($\lambda_1 \neq \lambda_2$)

Alternating pulses of the photon sources, as shown in Figure 5A, provided the possibility for more efficient use of photons. The coordination of photons via pulsing occurred over a period of time, τ_{coord}, comprising blue (Δt_1) and red (Δt_2), with coordination frequency, $f_{coord} = 1/\tau_{coord}$. The DC was defined as the fraction of time wavelength i comprising the total period, $DC_i = \Delta t_i/\tau_{coord}$. As the light source of each individual wavelength (λ_1 or λ_2) was produced as a Poisson distribution of temporally spaced photons, the temporal difference between each photon of the same wavelength (Δt,ph$_1$ or Δt,ph$_2$) within a period also yielded a Poisson distribution.

The system of alternating light sources has several variables that can be tuned to maximize the fraction of mixed-wavelength photon pairs that arrive at the surface; these parameters include the individual photon arrival frequencies ($f_{\text{arrival},1}$ and $f_{\text{arrival},2}$), the coordination frequency (f_{coord}), the DC (DC_1), and all of the reaction condition parameters (e.g., T, P, and X_{ss}). For the selected system at 100 bar, 1% conversion, and 338 K, the arrival frequencies of each of the individual light sources were selected as 100 Hz to ensure that simulations occurred in kinetic region IV of Figure 4B and because this region was already determined to exhibit the maximum kinetic benefit of light. Additionally, the DC was selected as a DC_1 of 50%, providing equal time for each light source to illuminate the surface. The resulting variable of interest remained the coordination frequency, f_{coord}.

The simulated sequence of photons with two different wavelengths arriving at the surface with non-zero coordination frequency was depicted in Figure 5B. For low coordination frequencies ($f_{\text{coord}} < f_{\text{arrival,i}}$), the majority of photon sequences were repetitions of the same wavelength. In this case, there were long periods of time where the same photon wavelength illuminated the catalyst surface. When the coordination frequency was comparable to the arrival frequencies ($f_{\text{coord}} = f_{\text{arrival,i}}$), the percentage of photons in series with the same wavelength was 50%. Most surprisingly, for coordination frequencies greater than the photon arrival frequency ($f_{\text{coord}} > f_{\text{arrival,i}}$), the percentage of repeated wavelength photons in series remained at 50% within statistical error.

The inability to increase the percentage of sequential photons with alternating wavelengths by coordinated pulsing of light sources resulted in a negligible photocatalytic kinetic benefit. As shown in Figure 5C, the TOF_B for low coordination frequency ($f_{\text{coord}} < 100$ Hz) was equal to a linear combination of the TOF_B of the two individual wavelengths of light under constant illumination; this system behaved as the average of two catalysts independently illuminated with the two different wavelengths of light. The surface coverages of A* and B* (Figure 5D) did not significantly change, and the QYs of both wavelengths (Figure 5E) were low. With a high fraction of sequential photons arriving at the catalyst surface with the same wavelength, most photons only generated heat and did not promote the reaction. Alternatively, for high coordination frequencies ($f_{\text{coord}} > 100$ Hz), the TOF_B achieved a maximum equal to the TOF_B of a catalyst illuminated continuously with both wavelengths of light (each at an $f_{\text{arrival,i}}$ of 50 Hz due to $DC_i = 50\%$). Moreover, the QYs of each wavelength achieved only ~50%, equal to the IQY_{total} of 50% (see Figure S10). The limited kinetic benefit of pulsing between two different-wavelength photons was consistent with the inherently dynamic nature of illuminated catalyst surfaces. A CW light source actually comprises individual photons; the apparent constant nature of a light source is the interpretation of the experimenter.[43] The catalyst active site experiences dynamic promotion via light under all circumstances of photon generation, independent of the extent of coordination of the light source via pulsing or chopping. As such, continuous illumination provides a catalytic rate enhancement equal to or better than coordinated light sources. This significant insight is supported by the nature and timescales of photon interactions with photocatalytic materials. The lifetime of excited states (fs) is much faster than the effect of local photon-generated heat (ps – ns) and is much faster than the timescales of the coordinated light sources considered here.

DISCUSSION

The simulations provide a framework to evaluate—using a simplified model—the boundaries of QYs in photon-driven thermal catalysis. Considering the practical application of such a catalytic system, the cost for photon production must be considered.[20,44] Especially for the generation of photons of specific wavelengths, an artificial light source would be commonly used. Our analysis shows that despite the model conditions of an IQY for a single elementary step of 100%, overall IQYs can significantly decrease in two-photon processes due to an unfavorable distribution of site occupancy in certain operational regimes. This is especially remarkable as the studied simulation represents an idealized system without considering (1) external factors such as reaction cell, light scattering in the reactor by reaction medium, and catalyst, nor (2) light absorption probability of the catalyst and the actual utilization of the absorbed photon. Both factors strongly reduce the apparent QY of photocatalysts.

The simulations conducted here provide two distinct kinetic signatures that can have broad utility for understanding the use of light to promote industrial surface chemistry. For example, for light applied to any reaction, it is not immediately obvious if photons promote only a single or multiple rate-controlling elementary steps. It is also not immediately apparent if one or two different wavelengths of light are necessary to promote catalytic reactions beyond the Sabatier limit. A first kinetic signature of multi-step light enhancement relates to the accessible rates above a Sabatier volcano with light. For reactions for which light only enhances a single rate-controlling elementary step, the TOF_B can only accelerate reactions up to the edge of the inverted volcano (gray region of Figure 2B), defined by the dashed lines extending from the sides of the Sabatier volcano.[16] Alternatively, one or more wavelengths of light that promote two rate-controlling elementary steps can access rates inside the inverted volcano (Figure 2B). This is a distinct visual check on the photocatalytic activity of light.

A second kinetic signature of multi-step photocatalytic promotion exists in the shape of an Arrhenius plot. Surface reactions for which light accelerates only a single rate-controlling step exhibit three distinct kinetic regimes, of which the intermediate regime corresponds to a slope at or near zero for an Arrhenius plot.[16] Alternatively, photocatalytic reactions for which light accelerates the two dominant rate-controlling steps exhibit only two significant kinetic regimes (Figure 3A). At high temperatures, the slope of the Arrhenius plot is defined by the thermocatalytic rate, while at low temperatures, the Arrhenius plot is flat (or much less than the slope associated with thermocatalysis).[17] This difference between the two photocatalytic mechanisms (single-step or multi-step light promotion) becomes apparent as the temperature decreases and the rate either remains constant (multi-step light promotion) or decreases (single-step light promotion).

The utility of insights from the generic A(g)-to-B(g) photocatalytic reaction derives from the commonality of the

Sabatier volcano. Many important catalytic reactions exhibit a Sabatier maximum, including examples such as ammonia synthesis,[45–47] water splitting to form hydrogen,[48,49] decomposing energy carriers such as formic acid,[50,51] or the oxygen reduction reaction (ORR) for catalytic power systems or chemical production.[52,53] Enhancing the rate of these types of reactions using light requires the selection of light that interacts with specific surface intermediates relevant to rate-controlling reactions that define the Sabatier volcano. In addition, light must be applied at an appropriate flux and sequence to efficiently use light for rate enhancement. This means that the experimentally set light flux can be selected to achieve the photon arrival frequency (i.e., per-site photon flux) that achieves maximum catalytic performance in IQY and/or TOF based on the controlling kinetic regime.[54,55] The map of kinetic regimes (Figure 4) therefore serves as a general example of the efficiency and kinetic rate enhancement that could be achieved in real catalytic chemistries. It also guides the selection of illumination conditions[35] in emerging photocatalytic opportunities, including photoredox catalysts,[56,57] artificial photosynthesis and solar-to-fuel applications,[58] and photoelectrocatalysis,[54] where the significant complexity of integrated thermo-, electro-, and photochemistries requires fundamental understanding of the controlling reactions and external stimuli. Future work will expand the general photocatalytic models to these classes of real chemistries to understand the kinetic implications of many-photon catalytic processes.

METHODS

Simulations were conducted in MATLAB 2019a using the kMC model described in the kMC development section of the results and the code and model equations in the supplemental information file.

RESOURCE AVAILABILITY

Lead contact

Requests for further information and resources should be directed to and will be fulfilled by the lead contact, Paul Dauenhauer (hauer@umn.edu).

Materials availability

Not applicable.

Data and code availability

All code and data are available in the supplemental information.

- Simulation results data have been deposited in the supplemental information data file as tables. They are publicly available as of the date of publication.
- All original code is available in this paper's supplemental information.
- Any additional information required to reanalyze the data reported in this paper is available upon request.

ACKNOWLEDGMENTS

This work was supported as part of the Center for Programmable Energy Catalysis, an Energy Frontier Research Center funded by the US Department of Energy, Office of Science, Basic Energy Sciences, at the University of Minnesota under award #DE-SC0023464.

AUTHOR CONTRIBUTIONS

Writing, J.R.C., A.B., and P.J.D.; methodology, J.R.C. and P.J.D.; visualization, J.R.C. and P.J.D.; software, J.R.C. and P.J.D.; conceptualization, A.B. and P.J.D.; investigation, A.B. and P.J.D.; funding acquisition, P.J.D.

DECLARATION OF INTERESTS

We, the authors, have no competing interests to declare related to this work.

SUPPLEMENTAL INFORMATION

Supplemental information can be found online at https://doi.org/10.1016/j.xcrp.2026.103306.

Received: January 30, 2026
Revised: March 28, 2026
Accepted: April 13, 2026
Published: May 12, 2026

REFERENCES

1. Medford, A.J., Vojvodic, A., Hummelshøj, J.S., Voss, J., Abild-Pedersen, F., Studt, F., Bligaard, T., Nilsson, A., and Nørskov, J.K. (2015). From the Sabatier Principle to a Predictive Theory of Transition-Metal Heterogeneous Catalysis. J. Catal. *328*, 36–42. https://doi.org/10.1016/j.jcat.2014.12.033.
2. Balandin, A.A. (1964). The Multiplet Theory of Catalysis - Energy Factors in Catalysis. Russ. Chem. Rev. *33*, 258–275. https://doi.org/10.1070/rc1964v033n05abeh001407.
3. Vijh, A.K. (1973). Sabatier-Balandin Interpretation of the Catalytic Decomposition of Nitrous Oxide on Metal-Oxide Semiconductors. J. Catal. *31*, 51–54. https://doi.org/10.1016/0021-9517(73)90269-8.
4. Ardagh, M.A., Abdelrahman, O.A., and Dauenhauer, P.J. (2019). Principles of Dynamic Heterogeneous Catalysis: Surface Resonance and Turnover Frequency Response. ACS Catal. *9*, 6929–6937. https://doi.org/10.1021/acscatal.9b01606.
5. Canavan, J., Hopkins, J., Foley, B., Abdelrahman, O., and Dauenhauer, P. (2025). Catalytic Resonance Theory: Turnover Efficiency and the Resonance Frequency. ACS Catal *15*, 653–663. https://doi.org/10.1021/acscatal.4c06623.
6. Shetty, M., Walton, A., Gathmann, S.R., Ardagh, M.A., Gopeesingh, J., Resasco, J., Birol, T., Zhang, Q., Tsapatsis, M., Vlachos, D.G., et al. (2020). The Catalytic Mechanics of Dynamic Surfaces: Stimulating Methods for Promoting Catalytic Resonance. ACS Catal. *10*, 12666–12695. https://doi.org/10.1021/acscatal.0c03336.
7. Monai, M., Albrecht, W., Alkemper, A., Artrith, N., Baldi, A., Beck, A., Berry, R.T., Bianco, E., Brzesowsky, F.A., Dong, Q., et al. (2026). Grand Challenges and Opportunities in Stimulated Dynamic and Resonant Catalysis. ACS Catal *16*, 4077–4112. https://doi.org/10.1021/acscatal.5c07014.
8. Onn, T.M., Gathmann, S.R., Wang, Y., Patel, R., Guo, S., Chen, H., Soeherman, J.K., Christopher, P., Rojas, G., Mkhoyan, K.A., et al. (2022). Alumina Graphene Catalytic Condenser for Programmable Solid Acids. JACS Au *2*, 1123–1133. https://doi.org/10.1021/jacsau.2c00114.
9. Onn, T.M., Gathmann, S.R., Guo, S., Solanki, S.P.S., Walton, A., Page, B.J., Rojas, G., Neurock, M., Grabow, L.C., Mkhoyan, K.A., et al. (2022). Platinum Graphene Catalytic Condenser for Millisecond Programmable Metal Surfaces. J. Am. Chem. Soc. *144*, 22113–22127. https://doi.org/10.1021/jacs.2c09481.
10. Shetty, M., Ardagh, M.A., Pang, Y., Abdelrahman, O.A., and Dauenhauer, P.J. (2020). Electric-Field-Assisted Modulation of Surface Thermochemistry. ACS Catal. *10*, 12867–12880. https://doi.org/10.1021/acscatal.0c02124.

11. Che, F., Gray, J.T., Ha, S., Kruse, N., Scott, S.L., and McEwen, J.-S. (2018). Elucidating the Roles of Electric Fields in Catalysis: A Perspective. ACS Catal. *8*, 5153–5174. https://doi.org/10.1021/acscatal.7b02899.
12. Khorshidi, A., Violet, J., Hashemi, J., and Peterson, A.A. (2018). How Strain Can Break the Scaling Relations of Catalysis. Nat. Catal. *1*, 263–268. https://doi.org/10.1038/s41929-018-0054-0.
13. Wintterlin, J., Zambelli, T., Trost, J., Greeley, J., and Mavrikakis, M. (2003). Atomic-Scale Evidence for an Enhanced Catalytic Reactivity of Stretched Surfaces. Angew. Chem. Int. Ed. *42*, 2850–2853. https://doi.org/10.1002/anie.200250845.
14. Qi, J., Resasco, J., Robatjazi, H., Alvarez, I.B., Abdelrahman, O., Dauenhauer, P., and Christopher, P. (2020). Dynamic Control of Elementary Step Energetics via Pulsed Illumination Enhances Photocatalysis on Metal Nanoparticles. ACS Energy Lett. *5*, 3518–3525. https://doi.org/10.1021/acsenergylett.0c01978.
15. Zhou, L., Swearer, D.F., Zhang, C., Robatjazi, H., Zhao, H., Henderson, L., Dong, L., Christopher, P., Carter, E.A., Nordlander, P., and Halas, N.J. (2018). Quantifying Hot Carrier and Thermal Contributions in Plasmonic Photocatalysis. Science *362*, 69–72. https://doi.org/10.1126/science.aat6967.
16. Canavan, J.R., and Dauenhauer, P.J. (2026). Catalytic Resonance Theory: Kinetics and Frequency Response of Light-Promoted Catalysis. Chem Catal. *6*, 101729. https://doi.org/10.1016/j.checat.2026.101729.
17. Beck, A., Gordon, M.J., and Christopher, P. (2026). Distinct Kinetic Signatures of Photodesorption from Metal Nanoparticles. J. Am. Chem. Soc. *148*, 7024–7034. https://doi.org/10.1021/jacs.5c17718.
18. Turner, J.J., George, M.W., Poliakoff, M., and Perutz, R.N. (2022). Photochemistry of Transition Metal Carbonyls. Chem. Soc. Rev. *51*, 5300–5329. https://doi.org/10.1039/D1CS00826A.
19. Perutz, R.N., and Procacci, B. (2016). Photochemistry of Transition Metal Hydrides. Chem. Rev. *116*, 8506–8544. https://doi.org/10.1021/acs.chemrev.6b00204.
20. Swierk, J.R. (2023). The Cost of Quantum Yield. Org. Process Res. Dev. *27*, 1411–1419. https://doi.org/10.1021/acs.oprd.3c00167.
21. Schubert, G., Bánsági, T., and Solymosi, F. (2025). Photocatalytic Decomposition of Methyl Formate over TiO_2-Supported Pt Metals. J. Phys. Chem. C *148*, 7024. https://doi.org/10.1021/jp406840n.
22. Plessow, P.N., and Abild-Pedersen, F. (2015). Examining the Linearity of Transition State Scaling Relations. J. Phys. Chem. C *119*, 10448–10453. https://doi.org/10.1021/acs.jpcc.5b02055.
23. Abild-Pedersen, F. (2016). Computational Catalyst Screening: Scaling, Bond-Order and Catalysis. Catal. Today *272*, 6–13. https://doi.org/10.1016/j.cattod.2015.08.056.
24. Jones, G., Bligaard, T., Abild-Pedersen, F., and Nørskov, J.K. (2008). Using Scaling Relations to Understand Trends in the Catalytic Activity of Transition Metals. J. Phys. Condens. Matter *20*, 064239. https://doi.org/10.1088/0953-8984/20/6/064239.
25. Canavan, J.R., Abdelrahman, O.A., Foley, B.L., and Dauenhauer, P.J. (2025). Catalytic Resonance Theory: Experimental and Kinetic Interpretation of Programmable Catalysis. ACS Catal. *15*, 17024. https://doi.org/10.1021/acscatal.5c03878.
26. Gillespie, D.T. (1976). A General Method for Numerically Simulating the Stochastic Time Evolution of Coupled Chemical Reactions. J. Comput. Phys. *22*, 403–434. https://doi.org/10.1016/0021-9991(76)90041-3.
27. Andersen, M., Panosetti, C., and Reuter, K. (2019). A Practical Guide to Surface Kinetic Monte Carlo Simulations. Front. Chem. *7*, 202. https://doi.org/10.3389/fchem.2019.00202.
28. Stamatakis, M., and Vlachos, D.G. (2011). A graph-theoretical kinetic Monte Carlo framework for on-lattice chemical kinetics. J. Chem. Phys. *134*, 214115. https://doi.org/10.1063/1.3596751.
29. Froment, G.F., Bischoff, K.B., and De Wilde, J. (2010). Chemical Reactor Analysis and Design, 3rd ed. (Wiley-VCH Verlag).
30. Jodłowski, P.J., Jędrzejczyk, R.J., Gancarczyk, A., Łojewska, J., and Kołodziej, A. (2017). New Method of Determination of Intrinsic Kinetic and Mass Transport Parameters from Typical Catalyst Activity Tests: Problem of Mass Transfer Resistance and Diffusional Limitation of Reaction Rate. Chem. Eng. Sci. *162*, 322–331. https://doi.org/10.1016/j.ces.2017.01.024.
31. Zhdanov, V.P. (2001). Pattern Formation in Catalytic Reactions Due to Lateral Adsorbate−Adsorbate Interactions. Langmuir *17*, 1793–1799. https://doi.org/10.1021/la001161j.
32. Li, X., and Grabow, L.C. (2022). Evaluating the Benefits of Kinetic Monte Carlo and Microkinetic Modeling for Catalyst Design Studies in the Presence of Lateral Interactions. Catal. Today *387*, 150–158. https://doi.org/10.1016/j.cattod.2021.03.010.
33. Christopher, P., Xin, H., and Linic, S. (2011). Visible-Light-Enhanced Catalytic Oxidation Reactions on Plasmonic Silver Nanostructures. Nat. Chem. *3*, 467–472. https://doi.org/10.1038/nchem.1032.
34. Braslavsky, S.E., Braun, A.M., Cassano, A.E., Emeline, A.V., Litter, M.I., Palmisano, L., Parmon, V.N., and Serpone, N. (2011). Glossary of terms used in photocatalysis and radiation catalysis (IUPAC Recommendations 2011). Pure Appl. Chem. *83*, 931–1014. https://doi.org/10.1351/PAC-REC-09-09-36.
35. Pashley-Johnson, F., Wu, X., Carroll, J.A., Walden, S.L., Frisch, H., Unterreiner, A.-N., Du Prez, F.E., Wagenknecht, H.-A., Read de Alaniz, J., Feringa, B.L., et al. (2025). Precision Photochemistry: Every Photon Counts. Angew. Chem. Int. Ed. *64*, e202502651. https://doi.org/10.1002/anie.202502651.
36. Devi, H.R., Bisen, O.Y., Nanda, S., Nandan, R., and Nanda, K.K. (2021). Internal versus External Quantum Efficiency of Luminescent Materials, Photovoltaic Cells, Photodetectors and Photoelectrocatalysis. Curr. Sci. *121*, 894–898.
37. Campbell, C.T. (2017). The Degree of Rate Control: A Powerful Tool for Catalysis Research. ACS Catal. *7*, 2770–2779.
38. Campbell, C.T., and Mao, Z. (2021). Analysis and Prediction of Reaction Kinetics Using the Degree of Rate Control. J. Catal. *404*, 647–660. https://doi.org/10.1016/j.jcat.2021.10.002.
39. Foley, B.L., and Bhan, A. (2020). Degree of Rate Control and De Donder Relations – An Interpretation Based on Transition State Theory. J. Catal. *384*, 231–251.
40. Foley, B.L., and Bhan, A. (2020). Degrees of Rate Control at Non(Pseudo)Steady-State Conditions. ACS Catal. *10*, 2556–2564. https://doi.org/10.1021/acscatal.9b04910.
41. Fox, M. (2006). *Quantum Optics: An Introduction*; Oxford Master Series in Physics (Oxford University Press).
42. Mandel, L., and Wolf, E. (1995). Optical Coherence and Quantum Optics (Cambridge University Press). https://doi.org/10.1017/CBO9781139644105.
43. Fowles, G.R. (1989). Introduction to Modern Optics, 2nd ed. (Dover Publications).
44. Schroeder, E., and Christopher, P. (2022). Chemical Production Using Light: Are Sustainable Photons Cheap Enough? ACS Energy Lett. *7*, 880–884. https://doi.org/10.1021/acsenergylett.2c00142.
45. Ichikawa, S. (1990). Volcano-Shaped Curves in Heterogeneous Catalysis. Chem. Eng. Sci. *45*, 529–535. https://doi.org/10.1016/0009-2509(90)87039-U.
46. Wang, T., and Abild-Pedersen, F. (2021). Achieving Industrial Ammonia Synthesis Rates at Near-Ambient Conditions through Modified Scaling Relations on a Confined Dual Site. Proc. Natl. Acad. Sci. USA *118*, e2106527118. https://doi.org/10.1073/pnas.2106527118.
47. Wittreich, G.R., Vlachos, D.G., Liu, S., and Dauenhauer, P.J. (2022). Catalytic Resonance of Ammonia Synthesis by Simulated Dynamic Ruthenium Crystal Strain. Sci. Adv. *8*, eabl6576. https://doi.org/10.1126/sciadv.abl6576.
48. Man, I.C., Su, H.Y., Calle-Vallejo, F., Hansen, H.A., Martínez, J.I., Inoglu, N.G., Kitchin, J., Jaramillo, T.F., Nørskov, J.K., and Rossmeisl, J. (2011).

Universality in Oxygen Evolution Electrocatalysis on Oxide Surfaces. ChemCatChem *3*, 1159–1165. https://doi.org/10.1002/cctc.201000397.

49. Gathmann, S.R., Bartel, C.J., Grabow, L.C., Abdelrahman, O.A., Frisbie, C.D., and Dauenhauer, P.J. (2024). Dynamic Promotion of the Oxygen Evolution Reaction via Programmable Metal Oxides. ACS Energy Lett. *9*, 2013–2023.
50. Tang, Y., Roberts, C.A., Perkins, R.T., and Wachs, I.E. (2016). Revisiting Formic Acid Decomposition on Metallic Powder Catalysts: Exploding the HCOOH Decomposition Volcano Curve. Surf. Sci. *650*, 103–110. https://doi.org/10.1016/j.susc.2015.12.032.
51. Gopeesingh, J., Ardagh, M.A., Shetty, M., Burke, S.T., Dauenhauer, P.J., and Abdelrahman, O.A. (2020). Resonance-Promoted Formic Acid Oxidation via Dynamic Electrocatalytic Modulation. ACS Catal. *10*, 9932–9942. https://doi.org/10.1021/acscatal.0c02201.
52. Urrego-Ortiz, R., Almeida, M.O., and Calle-Vallejo, F. (2024). Error Awareness in the Volcano Plots of Oxygen Electroreduction to Hydrogen Peroxide. ChemSusChem *17*, e202400873. https://doi.org/10.1002/cssc.202400873.
53. Sargeant, E., Illas, F., Rodríguez, P., and Calle-Vallejo, F. (2022). On the Shifting Peak of Volcano Plots for Oxygen Reduction and Evolution. Electrochim. Acta *426*, 140799. https://doi.org/10.1016/j.electacta.2022.140799.
54. Wadsworth, B.L., Beiler, A.M., Khusnutdinova, D., Reyes Cruz, E.A., and Moore, G.F. (2019). Interplay between Light Flux, Quantum Efficiency, and Turnover Frequency in Molecular-Modified Photoelectrosynthetic Assemblies. J. Am. Chem. Soc. *141*, 15932–15941. https://doi.org/10.1021/jacs.9b07295.
55. Nishiori, D., Hensleigh, L.K., Nguyen, N.P., Peterson, I., and Moore, G.F. (2025). Wavelength-Resolving Catalytic Turnover Frequencies and Identifying Alternate Proton Donors in Solar-Fuel-Forming Reactions. ACS Catal. *15*, 6361–6371. https://doi.org/10.1021/acscatal.4c07140.
56. De Kreijger, S., Glaser, F., and Troian-Gautier, L. (2024). From Photons to Reactions: Key Concepts in Photoredox Catalysis. Chem Catal. *4*, 101110. https://doi.org/10.1016/j.checat.2024.101110.
57. Romero, N.A., and Nicewicz, D.A. (2016). Organic Photoredox Catalysis. Chem. Rev. *116*, 10075–10166. https://doi.org/10.1021/acs.chemrev.6b00057.
58. Reyes Cruz, E.A., Nishiori, D., Wadsworth, B.L., Nguyen, N.P., Hensleigh, L.K., Khusnutdinova, D., Beiler, A.M., and Moore, G.F. (2022). Molecular-Modified Photocathodes for Applications in Artificial Photosynthesis and Solar-to-Fuel Technologies. Chem. Rev. *122*, 16051–16109. https://doi.org/10.1021/acs.chemrev.2c00200.